applied sciences

MDPI

Article

Multiscale Characterization of Fractures and Analysis of Key Controlling Factors for Fracture Development in Tight Sandstone Reservoirs of the Yanchang Formation, SW Ordos Basin, China

Peng Chen [1,2], Shuhan Yang [1,2], Xinyu Chen [1,2], Zeyu Li [1,2], Chuanbo Shen [1,2] and Huaning Qiu [1,2,*]

[1] School of Earth Resources, China University of Geosciences, Wuhan 430074, China
[2] Key Laboratory of Tectonics and Petroleum Resources, Ministry of Education, China University of Geosciences, Wuhan 430074, China
* Correspondence: huaningqiu@cug.edu.cn; Tel.: +86-13312887168

Abstract: Tight sandstone reservoirs, despite their low porosity and permeability, present considerable exploration potential as unconventional hydrocarbon resources. Natural fractures play a crucial role in hydrocarbon migration, accumulation, and present engineering challenges such as late-stage reformation in these reservoirs. This study examines fractures in the seventh member of the Triassic Yanchang Formation's tight sandstone within the Ordos Basin using a range of methods, including field outcrops, core samples, imaging and conventional logging, thin sections, and scanning electron microscopy. The study clarifies the characteristics of fracture development and evaluates the relationship between dynamic and static rock mechanics parameters, including the calculation of the brittleness index. Primary factors influencing fracture development were quantitatively assessed through a combination of outcrop, core, and mechanical test data. Findings reveal that high-angle structural fractures are predominant, with some bedding and diagenetic fractures also present. Acoustic, spontaneous potential, and caliper logging, in conjunction with imaging data, enabled the development of a comprehensive probabilistic index for fracture identification, which produced favorable results. The analysis identifies four key factors influencing fracture development: stratum thickness, brittleness index, lithology, and rock mechanical stratigraphy. Among these factors, stratum thickness is negatively correlated with fracture development. Conversely, the brittleness index positively correlates with fracture development and significantly influences fracture length, aperture, and linear density. Fractures are most prevalent in siltstone and fine sandstone, with minimal development in mudstone. Different rock mechanics layer types also impact fracture development. These insights into fracture characteristics and controlling factors are anticipated to enhance exploration efforts and contribute to the study of similar unconventional reservoirs.

Keywords: tight sandstone reservoirs; fracture identification; main controlling factors; Ordos Basin; Yanchang Formation

check for updates

Citation: Chen, P.; Yang, S.; Chen, X.; Li, Z.; Shen, C.; Qiu, H. Multiscale Characterization of Fractures and Analysis of Key Controlling Factors for Fracture Development in Tight Sandstone Reservoirs of the Yanchang Formation, SW Ordos Basin, China. *Appl. Sci.* **2024**, *14*, 9676. https://doi.org/10.3390/app14219676

Academic Editor: Tiago Miranda

Received: 13 September 2024
Revised: 15 October 2024
Accepted: 18 October 2024
Published: 23 October 2024

Copyright: © 2024 by the authors. Licensee MDPI, Basel, Switzerland. This article is an open access article distributed under the terms and conditions of the Creative Commons Attribution (CC BY) license (https://creativecommons.org/licenses/by/4.0/).

1. Introduction

The decline in conventional oil and gas exploitation has led to increased attention toward unconventional oil and gas reservoirs [1–4]. Tight sandstone reservoirs, such as those within the Chang 7 member of the Upper Triassic Yanchang Formation in the Ordos Basin, China, are distinguished by extensive fracture development [5–8]. These fractures notably influence the "sweet spots" within the reservoir. Although fractures may not significantly increase the reservoir space in low-permeability sandstones, they substantially affect the connectivity of the reservoir [9]. The presence of natural fractures is crucial for guiding subsequent hydraulic and artificial fracturing processes, making the study of fractures in tight sandstone highly valuable [2,10,11].

Although previous studies have thoroughly analyzed the structural and sedimentary aspects of the Yanchang Formation [7,8,12], research on fractures within the Chang 7 member

remains inadequately systematic and in-depth. Several issues persist, including the reliance on single-scale data for fracture characterization, which has led to a limited understanding of fracture development. Earlier research on fractures in the tight sandstone of the seventh member of the Yanchang Formation was based on core descriptions or thin sections [6,13,14]. The scale used for describing and characterizing fractures in tight sandstone has been overly narrow, resulting in an unclear understanding of fracture development characteristics across various scales. Furthermore, a single logging curve demonstrates limited effectiveness in fracture identification, which can introduce uncertainty when employing conventional logging methods [15–17]. Although imaging logging offers relatively accurate fracture identification, it is costly and impractical to apply to every well [18]. Accurate identification of fractures through conventional logging curves is an urgent issue that must be resolved in tight sandstone reservoirs. Additionally, earlier studies have only provided qualitative analyses of the primary controlling factors affecting fracture development in tight sandstone, with quantitative factors remaining unclear. These limitations impede a comprehensive understanding of fracture distribution and development.

Given the current situation, the primary issue with characterizing fractures in tight sandstone is the overly narrow scale of analysis. Moreover, the high cost of imaging logging, though accurate, limits its application across all wells, contributing to gaps in understanding fracture characteristics on a broader scale [19]. Additionally, while various factors influence fracture development in tight sandstone, research into the primary controlling factors has been limited, further complicating efforts to enhance resource extraction [18,20]. To address these issues, it is essential to identify and characterize fractures across multiple scales and quantitatively determine the primary controlling factors of fracture development [21]. Our study aims to integrate imaging logging data from selected areas with conventional logging, allowing for the delineation of fracture development segments within the study area. This study offers a more comprehensive characterization of fractures in the tight sandstone of the Chang 7 member, providing a clearer understanding of their development. Additionally, we will investigate the primary controlling factors of fracture development in tight sandstone reservoirs.

This study is of high importance, as it seeks to fill the existing knowledge gaps in fracture characterization within the Yanchang Formation's tight sandstone reservoirs [5,6]. By integrating multi-scale data, this research will provide a more accurate and systematic understanding of fracture development and controlling factors. Such insights will contribute to the optimization of hydraulic fracturing techniques, enhancing the effective development of tight oil resources [22,23].

2. Geological Settings

The Ordos Basin is the second-largest petroliferous basin in China [11,12]. Situated in northern China, it is characterized by its rich oil and gas resources and complex geological structure [11,13,24,25]. This study focuses on the Xi 233 well area, located in the southwestern part of the Ordos Basin (Figure 1a). The overall structural setting is relatively simple, primarily featuring a large monocline with a gentle dip angle and minimal structural variations. The target layer for this study is the tight sandstone of the Chang 7 member of the Upper Triassic Yanchang Formation, within a sedimentary environment primarily influenced by deep-water gravity flow sedimentation in semi-deep to deep lake facies [7,8].

As a cratonic basin, the Ordos Basin exhibits stable subsidence and relatively undisturbed strata [6,7,12]. However, due to subsequent tectonic activity, some areas exhibit missing strata. The thickness of the Yanchang Formation is generally greater than 1000 m but less than 1500 m [26]. The Yanchang Formation is divided into ten sections from bottom to top (Figure 1b). This study focuses on the seven sections that primarily feature sedimentation ranging from semi-deep lake to deep lake facies.

In the Ordos Basin, the distribution of oil and gas is characterized as 'upper oil and lower gas' [12,24,27]. This means that Mesozoic hydrocarbons in the basin predominantly occur as petroleum, while Paleozoic hydrocarbons are primarily found as natural gas.

During the Paleozoic era in the Ordos Basin, the sedimentary environment gradually shifted from marine to marine–terrestrial transitional sedimentation [8,26,28]. By the end of the Late Paleozoic, marine sedimentation had ceased, and the basin began transitioning to predominantly terrestrial sedimentation. Within the Upper Triassic Yanchang Formation, thick and high-quality source rocks are observed at the base of the seventh member [14]. This stratum represents the optimal phase of lake basin development, and a significant portion of the Mesozoic oil and gas in the Ordos Basin is associated with it.

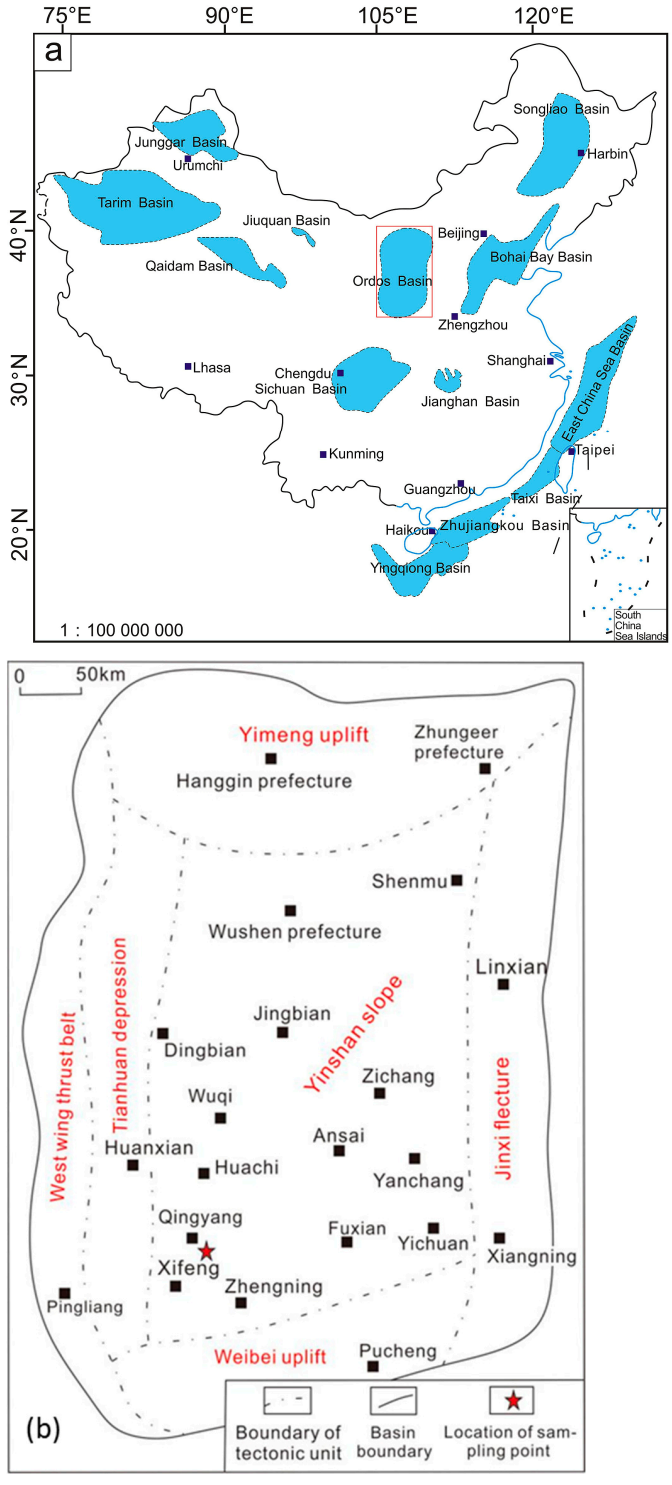


Figure 1. *Cont.*

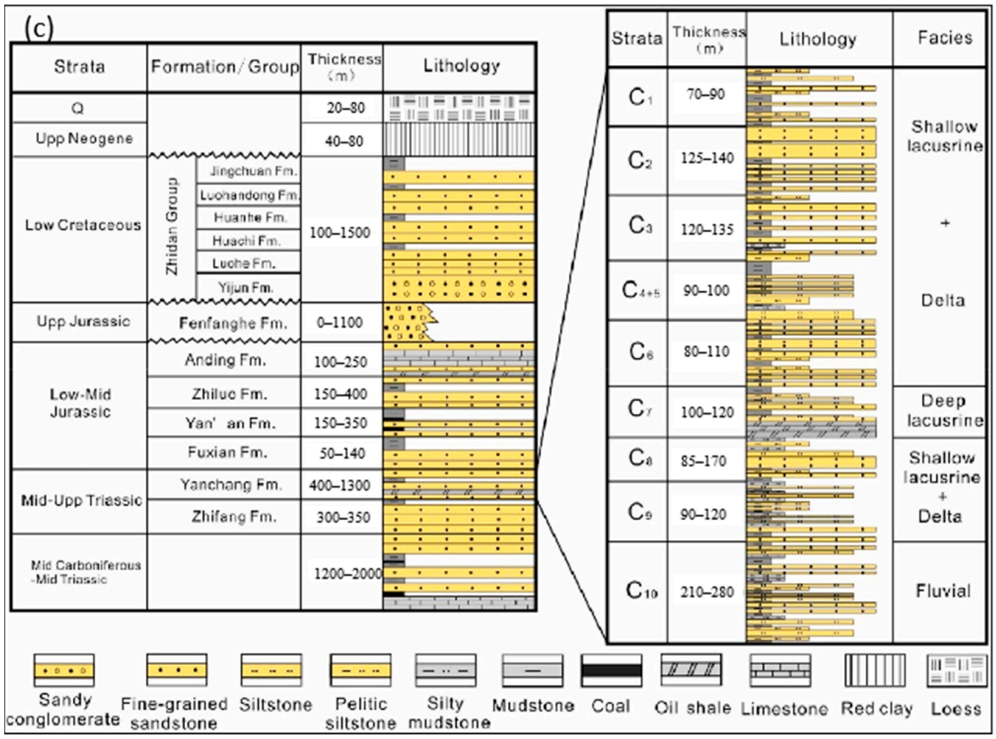


Figure 1. (**a**) Geographical location of the Ordos Basin Region. (**b**) Geographical location of the Xi 233 well site (the sampling point is located at the Xi 233 well site). (**c**) Stratigraphic unit of Yanchang Formation in the Xi 233 well area (C_7 stands for Chang 7 member of Yanchang Formation, and other formation codes follow this convention) [25].

3. Methods

3.1. Multiscale Approaches to Fracture Identification

Macroscopic fractures can be identified through seismic surveys, rock cores, and logging well, with sizes typically ranging from several hundred meters to a few centimeters [20,29]. Microscopic fractures can be identified using thin sections and scanning electron microscopy, ranging in size from micrometers to nanometers [23,30]. Fractures are categorized into structural and non-structural types [21,31]. Analyzing fracture characteristics at the outcrop and rock core scales facilitates the identification of fracture types, evaluation of fracture effectiveness, and measurement of parameters such as dip angle, opening, and length.

Imaging logging exhibits characteristics of high wellbore coverage and longitudinal resolution. The high-definition images of the wellbore wall provided by imaging logging can intuitively and accurately display the development of fractures. It is currently the most effective logging technology for the detailed identification and evaluation of fractures. In imaging logging images, fractures are typically displayed as sine curves, where the width of the curve indicates fracture opening, the orientation of the lowest point indicates fracture inclination, the amplitude indicates fracture dip angle, and the color reflects fracture filling conditions [18]. Generally, fractures with larger dip angles exhibit greater amplitudes in imaging logging data, whereas fractures with smaller dip angles display smaller amplitudes. Unfilled fractures typically appear as sinusoidal dark, high-conductivity features on imaging logs, as they often fill with mud during the logging process. Filled fractures exhibit higher resistance compared to the surrounding rock, resulting in bright, high-resistance features on imaging logs [18]. Microfractures identified via thin sections and scanning electron microscopy are strongly associated with diagenesis and tectonic activity. Thus, studying microfractures is crucial.

3.2. Comprehensive Probabilistic Method for Fracture Identification

The primary challenge in identifying fractures using a single conventional logging lies in the inherent limitations of fracture interpretation accuracy [15,32,33]. Since outliers on a logging curve arise from multiple interacting factors, fracture interpretation is intrinsically ambiguous [17,19]. Consequently, relying on a single conventional logging curve for fracture interpretation is challenging; thus, integrating multiple logging curves is essential [15,34]. A comprehensive fracture analysis was conducted by integrating multiple conventional logging curves:

(1) Conventional logging curves are selected to identify fracture development, and using the fracture identification criteria of each logging curve, the effective thickness h_i of the fracture development is determined through conventional logging.
(2) The actual thickness H_i of fracture development in the well section containing imaging logging data was measured, and the identified fracture thickness was confirmed to be accurate.
(3) The ratio p_i between the effective thickness and actual thickness is calculated.
(4) The reliability of fracture identification for each conventional logging curve is calculated:

$$m_i = \frac{p_i}{\sum_{i=1}^{m} p_i} \tag{1}$$

where m_i represents the reliability of any logging curve, defined as the weight of the curve; p_i denotes the fracture thickness identified through imaging logging.
(5) The logging curves are normalized to eliminate the influence of various dimensions:

$$x_i = \frac{X - X_{min}}{X_{max} - X_{min}} \tag{2}$$

where x_i represents the normalized conventional logging, X is the value at any point on the conventional log, X_{min} is the minimum value, and X_{max} is the maximum value of the conventional log.
(6) Based on the normalized values of conventional logging curves, a weighted average is calculated, yielding a new value referred to as the comprehensive probabilistic index:

$$P_i = \sum_{i=1}^{m} m_i \cdot x_i \tag{3}$$

where P_i denotes the comprehensive probabilistic index; x_i represents the normalized conventional logging; and m_i is the weight of the logging curve. Thus, a higher value of the comprehensive probability parameter signifies more developed fractures at that location.

3.3. Derivation of Rock Mechanics Parameters

There are generally two approaches to acquiring rock mechanics parameters. One approach involves statically determining rock mechanics parameters by observing rock deformation under controlled confining pressure in the laboratory [5,35]. The alternative approach involves using logging data to establish continuous dynamic profiles of rock mechanics parameters [35]. Static mechanical parameters measured in the laboratory simulate the magnitude of confining pressure during rock formation, the rate and amplitude of pressure loading, and the pressure changes during subsequent formation stages. Consequently, laboratory-measured static mechanical parameters provide a more accurate representation of the true mechanical properties of rocks [36,37]. A plunger sample with a diameter of 2.5 cm and a height of 5 cm was selected for rock mechanics experiments. The experimental equipment was commissioned to the Institute of Rock and Soil Mechanics, Chinese Academy of Sciences for measurement. The test standards adopted for this experiment are Part 7 of GB/T 23561.7-2009 [38] and Part 8 of GB/T 23561.8-2009 [39]: Methods for determining the uniaxial compressive strength and deformation parameters of coal and rock. The triaxial mechanical parameters of tight sandstone from the Chang 7 member

were measured using a digital triaxial testing machine with a load capacity ranging from 100 to 400 kN. The testing was conducted under either displacement or pressure control, and a high-precision pressure sensor, capable of measuring up to 100 MPa with an accuracy of ±0.1%, was used. Displacement measurements were recorded with a sensor that had a resolution of 0.001 mm or higher. The temperature during testing was maintained between 20 °C and 80 °C, with a precision of ±0.1 °C. Axial stress was applied at a rate of 0.01 to 0.1 MPa/s, while confining pressures were set at 0, 5, 10, and 15 MPa. Data acquisition was conducted in real time using a high-frequency system. However, measuring rock mechanics parameters in the laboratory necessitates sample preparation and incurs relatively high costs [40]. Given the unique characteristics of rock samples, it is necessary to obtain multiple samples. Acquiring dynamic rock mechanics parameters through logging conserves financial and material resources and enables the creation of continuous rock mechanics profiles. Therefore, investigating the relationship between dynamic and static rock mechanics parameters is essential [41]. Typically, static rock mechanics parameters obtained in the laboratory are used to calibrate dynamic parameters. The method for acquiring dynamic rock mechanics parameters is as follows:

$$E_d = \rho {v_s}^2 \frac{3{v_p}^2 - 4{v_s}^2}{{v_p}^2 - {v_s}^2} \tag{4}$$

$$\mu_d = \frac{{v_p}^2 - 2{v_s}^2}{2\left({v_p}^2 - {v_s}^2\right)} \tag{5}$$

where E_d is the dynamic Young's modulus, Gpa; μ_d is the dynamic Poisson's ratio; v_s is the shear wave velocity, m/μs; v_p is the compressional velocity, m/μs; and ρ is the rock density, kg/m^3.

3.4. Quantitative Assessment of Brittleness Index

Current research has identified twenty to thirty methods for calculating the rock brittleness index, each with specific conditions and characteristics [41–43]. A high brittleness index indicates more developed fractures that are more prone to later fracturing, whereas a low brittleness index suggests underdeveloped fractures, making subsequent fracturing less likely [43–45].

The commonly used methods for calculating the brittleness index include the rock mineral composition method and the mechanical parameter evaluation method [44]. The rock mineral composition method assesses the brittleness index based on the content of brittle minerals in rocks. Commonly used brittle minerals include quartz and feldspar, which are evaluated based on their percentages of the total mineral content:

$$BI = \frac{c_Q + c_F}{c_Q + c_F + c_C + c_M} \tag{6}$$

where BI denotes the brittleness index obtained from experiments; c_Q is the quartz content; c_F is the feldspar content; c_C is the carbonate content; c_M is the clay mineral content.

The brittleness index is calculated using rock mechanics parameters based on the principle that external pressure induces fractures, thereby altering the rock's mechanical properties [46]. Representative parameters include Young's modulus and Poisson's ratio [16,35,47]. Poisson's ratio indicates the change in rock strain under external pressure, while Young's modulus reflects the rock's resistance to fracturing [48,49]. Therefore, the combination of these parameters is significant for evaluating rock brittleness. The normalized Young's modulus (E_{nor}) and normalized Poisson's ratio (μ_{nor}) were utilized to calculate the brittleness index (BI_{nor}):

$$BI_{nor} = \frac{E_{nor} + \mu_{nor}}{2} \tag{7}$$

$$E_{nor} = \frac{E - E_{min}}{E_{max} - E_{min}} \quad (8)$$

$$\mu_{nor} = \frac{\mu_{max} - \mu}{\mu_{max} - \mu_{min}} \quad (9)$$

where BI_{nor} represents the normalized brittleness index obtained from logging curve calculations; E_{nor} is the normalized Young's modulus; μ_n is the normalized Poisson's ratio; E_{max} is the maximum value of static Young's modulus, GPa; E_{min} is the minimum value of static Young's modulus, GPa; $\mu_{\max}$ is the maximum value of static Poisson's ratio; $\mu_{\min}$ is the minimum value of static Poisson's ratio.

3.5. Rock Mechanical Stratigraphy Classification

The rock mechanics layer is defined as a continuous rock unit with homogeneous mechanical properties, bounded by distinct upper and lower limits. The most apparent differences between rock mechanics layers are manifested in parameters such as fracture density, spacing, and occurrence [36]. Currently, rock mechanics layers can be categorized using methods such as deformation, petrological, sequence stratigraphy, and rock mechanics parameter approaches. This study employs the rock mechanics parameter method to delineate rock mechanics layers, utilizing the brittleness index as the primary indicator [36,50,51]. Based on the definition of rock mechanics layers and analogous well logging interpretations, the midpoint of the brittleness index is used as a reference. When adjacent marker points exhibit similar mechanical parameters, they are grouped into the same rock mechanics layer.

4. Results

4.1. Fracture Characteristics Across Diverse Scales

The Chang 7 member of the Yanchang Formation in the Ordos Basin is distinguished by the development of tight sandstone [16,17]. Observations of outcrops in the Xi 233 well area and its surrounding regions reveal that the development is predominantly characterized by structural fractures (Figure 2A). Shear fractures typically display stable occurrences, extensive lengths, relatively planar surfaces, and substantial inclination angles, with some occurring as conjugate pairs [52,53]. The fractures observed in the target layer and its surrounding areas are predominantly high-angle shear fractures and vertical fractures, reflecting pronounced shear effects (Figure 2B). The angles of the conjugate fractures are generally around 60° (Figure 2C,D). Multiple periods of tectonic activity in the region have resulted in intersecting fractures visible in field outcrops (Figure 2A). Some fractures are significantly filled with calcite, pyrite, and mud, occupying space within oil and gas reservoirs (Figure 2E,F). However, the limited number of filled fractures in the region minimally impacts subsequent oil and gas accumulation [22].

Based on field outcrop observations and rock core fracture analysis, fractures in the study area are categorized into three types: structural fractures, bedding fractures, and diagenetic fractures [54,55].

(1) Structural fracture: Fractures formed under structural stress [21]. The Chang 7 member of the Yanchang Formation was deposited during the Indochina Movement, and the compressional forces from this tectonic event induced the formation of structural fractures. Fractures resulting from tectonic activity significantly alter the pore structure of the rock, increasing permeability, which facilitates the migration and accumulation of hydrocarbons. The high-angle shear fractures observed in the cores from the research area are elongated, with some core cross-sections exhibiting slickenside, indicating slippage at those locations (Figure 3A–C).

(2) Bedding fracture: A fracture formed by tectonic stress superimposed on pre-existing diagenetic fractures [21,52]. The research area exhibits numerous visible bedding fractures, which are often concentrated and densely developed (Figure 3D,E).

(3) Diagenetic fracture: A fracture formed during sedimentation or diagenesis, typically characterized by low angles [52]. Diagenetic processes, occurring under high temperature and pressure, can also generate fractures in the rock. Chemical and physical changes such as mineral dissolution, cement precipitation, or expansion of the rock may lead to fracture formation. These processes reduce rock strength, making it more susceptible to fracturing, while also affecting the rock's reservoir capacity. These fractures often occur at lithological boundaries and are visible in the study area but have a limited distribution (Figure 3F).

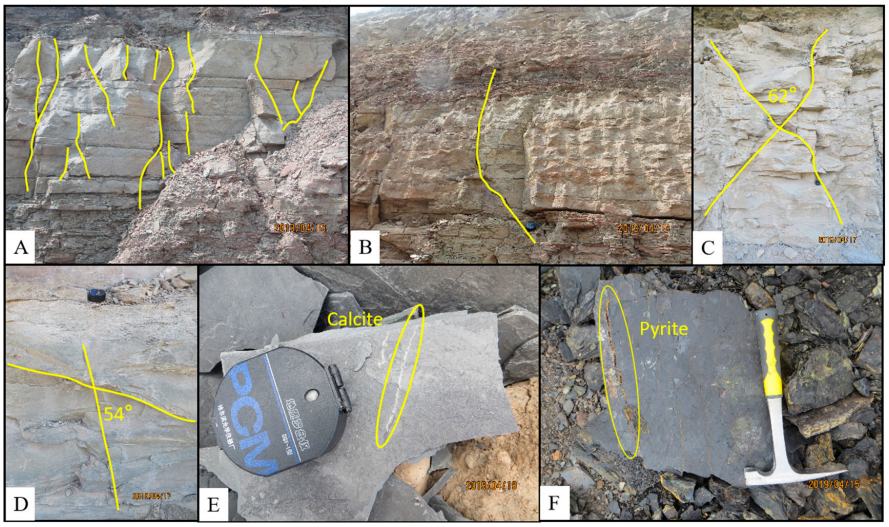


Figure 2. Detailed analysis of fracture development characteristics in field outcrops. (**A**) A network system composed of multiple high-angle shear fractures; (**B**) a single shear fracture extending over considerable distances; (**C**,**D**) the angles of the conjugate shear fractures are 62° and 54°, respectively; (**E**) the fracture-filling material is calcite; (**F**) the filling material within the fracture network system is pyrite.

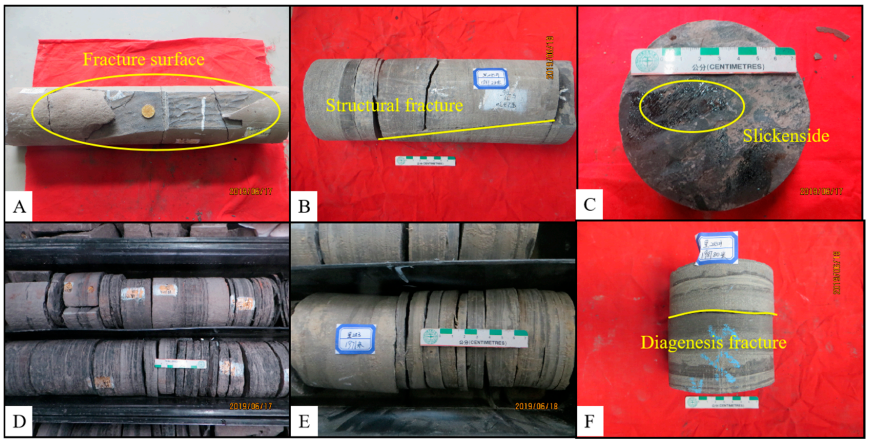


Figure 3. Fracture development characteristics in rock cores. (**A**,**B**) High-angle structural fractures; (**C**) slickenside; (**D**,**E**) horizontal bedding fractures; (**F**) diagenetic fractures caused by lithological interface changes.

By observing and describing the fractures in the rock core, the length, opening, dip angle, and filling degree of the structural fractures were statistically analyzed [55].

(1) Fracture length

Fracture lengths in the rock core are primarily distributed across three intervals: 10–20 cm, 20–30 cm, and 40–50 cm, accounting for 17%, 42%, and 15%, respectively (Figure 4A).

(2) Fracture aperture

The aperture of fractures is a crucial statistical parameter for characterizing them [52]. Fracture width significantly affects oil and gas migration and seepage. Observations and statistical results indicate that the fracture width in the core well primarily ranges from 0.05 to 0.5 mm (Figure 4B).

(3) Fracture dip

Due to the minimal inclination of the observed well, its impact on the fracture dip angle is negligible [5]. Consequently, the angle between the fracture and the wellbore axis can be considered the true dip angle. Based on the inclination angle, fractures can be categorized as vertical (75–90°), high-angle (45–75°), low-angle (15–45°), and horizontal (0–15°). Among these, high-angle and vertical fractures are predominant in the target layer of the core well (Figure 4C).

(4) Fracture filling degree

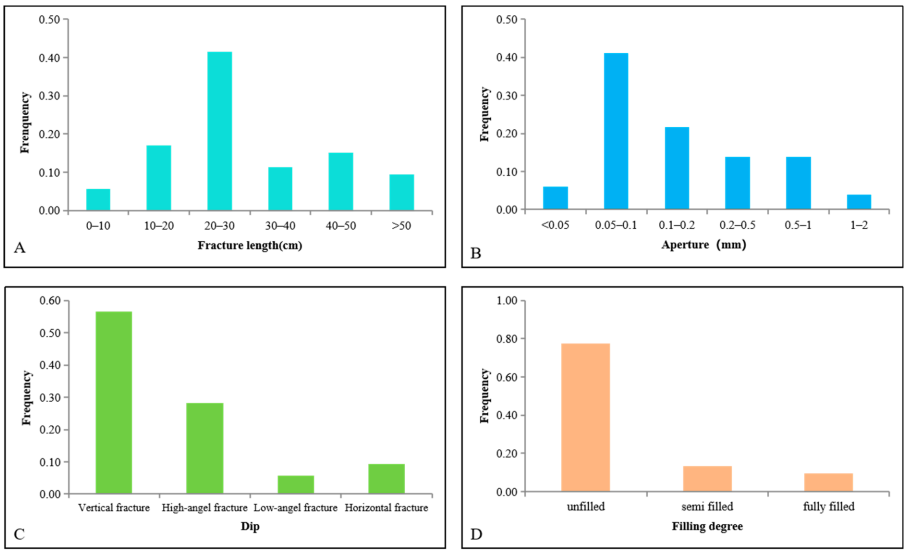


Figure 4. Histogram representing fracture development in rock cores. (**A**) Characteristics of fracture length. (**B**) Features of fracture aperture. (**C**) Aspects of fracture dip. (**D**) Details of fracture filling degree.

The degree of fracture filling, also referred to as fracture effectiveness, varies with the amount of filling material present [20]. Generally, fractures with minimal or no filling material exhibit higher effectiveness, whereas those with significant filling material have reduced effectiveness. In the cores, the overall degree of filling is relatively low, with most fractures remaining unfilled and only a small proportion being either filled or partially filled (Figure 4D).

Microscopic fracture identification focuses on fractures with apertures less than 0.1 mm, observable through thin sections and scanning electron microscopy [23,40]. Observations of rock thin sections and scanning electron microscopy reveal a significant number of microfractures in the Chang 7 member of the Yanchang Formation, predominantly intragranular, intergranular, and transgranular fractures (Figure 5A–F). Despite their small size, these fractures play a critical role in subsequent dissolution processes. Intragranular and intergranular fractures can develop secondary pores through dissolution processes [40,55]. Additionally, these fractures contain minimal filling material, making them effective storage spaces and significantly enhancing the physical properties of tight sandstone reservoirs [56].

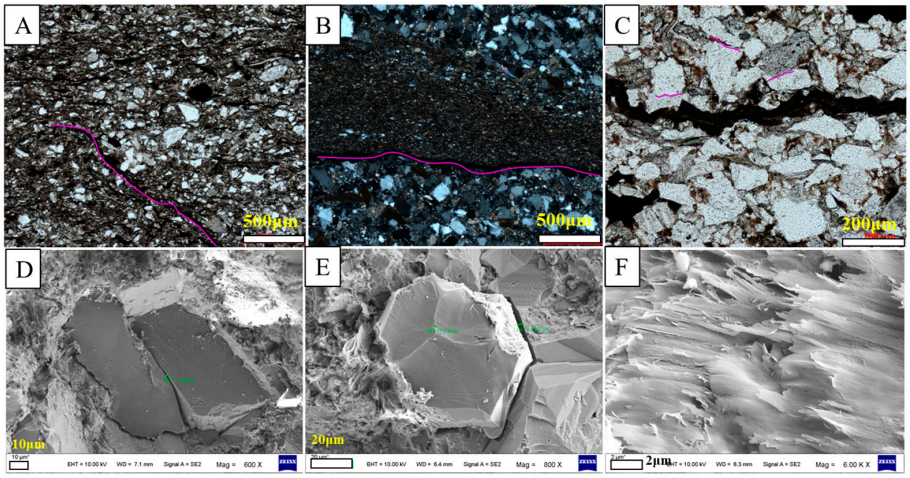


Figure 5. Microscopic characteristics of fracture development. (**A**) Transgranular fractures; (**B**) intergranular fractures; (**C**) intragranular fractures; (**D**) long columnar dolomite, development of intergranular fractures and dissolution pores; (**E**) microparticle quartz is concentrated and distributed, with intergranular fractures, shell-shaped fractures, and dissolution pores developed; (**F**) flake- and ribbon-shaped illite is distributed directionally, exhibiting well-developed pores and fractures.

Imaging logging is effective in identifying fractures but may also detect pseudo-fractures, such as induced fractures and layer interfaces [15,18]. Therefore, it is crucial to differentiate between genuine fractures and pseudo-fractures.

Imaging logging can identify both high-conductivity and high-resistance fractures, and roughly determine their dip angles [15,18]. Imaging logging data from the Xi 233 well area indicate that fractures in the Yanchang Formation are well-developed, particularly in the Chang 7 member, where high-angle fractures are predominant. Among the developed fractures, high-conductivity fractures are more common than high-resistance fractures, suggesting that most fractures are unfilled, consistent with field and core observations (Figure 6A,B). Additionally, each well in Chang 7 of the study area contains varying numbers of pseudo-fractures alongside natural fractures (Figure 6C–E).

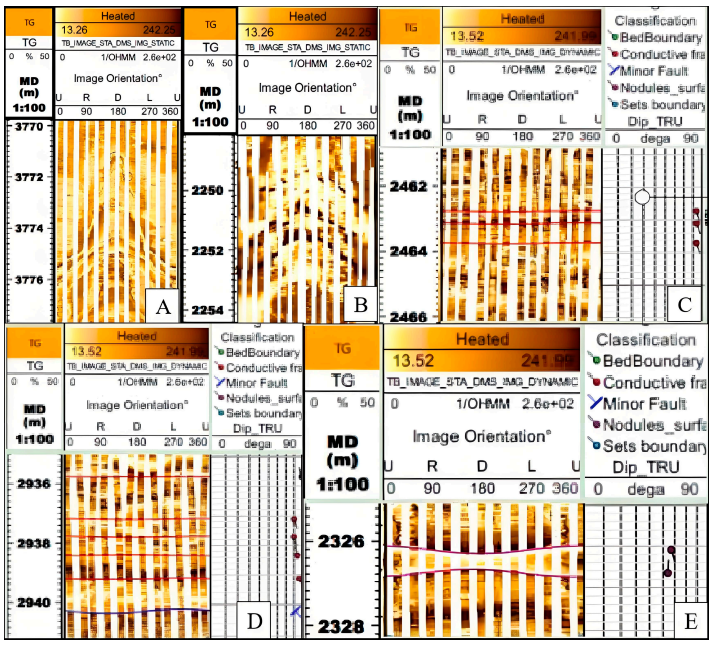


Figure 6. Characterization of various fractures using imaging logging. (**A**) High-resistance fractures; (**B**) high-conductivity fractures; (**C**) induced fractures; (**D**) small fault; (**E**) nodules.

4.2. Effect of Fracture Identification Using a Comprehensive Method

According to the comprehensive probability method, the contribution rate of each logging curve in the study area to the identification of fractures was calculated. Take its value as the weight coefficient and select appropriate logging curves as indicators to comprehensively determine the fractures. Based on the conditions of the Xi 233 well area, this study primarily selected three indicators: acoustic logging, spontaneous potential logging, and caliper logging for comprehensive fracture identification. Weights of 0.5, 0.3, and 0.2 were assigned based on their fracture identification effectiveness, and normalized logging curves were used to identify fractures.

Segments of fracture development in the target layer, identified using the comprehensive probability method, span 2135–2140 m and 2173–2181 m (Figure 7). In these segments, the maximum value of the comprehensive probability index P_f reaches 0.42 and 0.5, respectively. Collected data on fracture linear densities from the rock core and imaging logging reveal that fracture density in these segments is considerably high, reaching a maximum of 5.1/m. Consequently, determining fracture development segments using this method proves to be reliable, yielding favorable results.

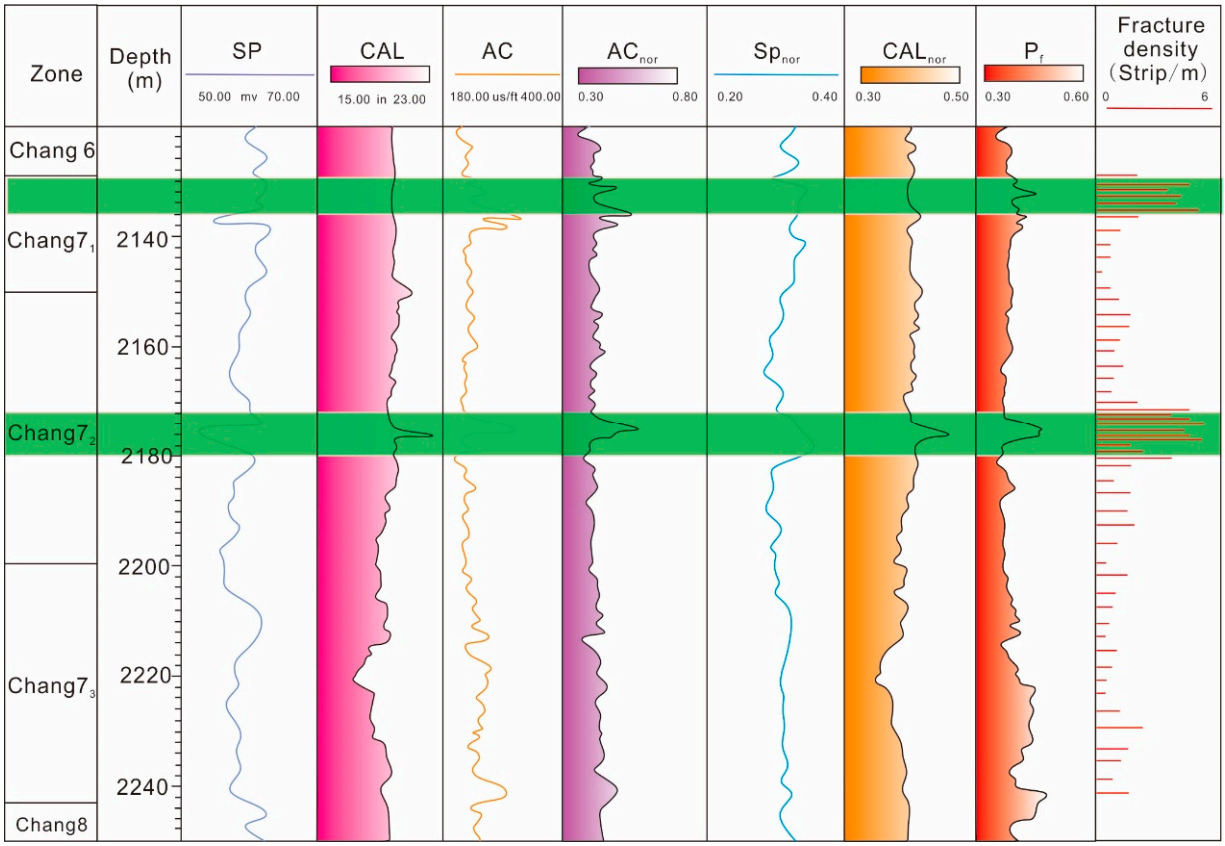


Figure 7. Effectiveness of fracture identification using the comprehensive probabilistic method (The green rectangle denotes the high fracture density.).

4.3. Conversion of Static to Dynamic Rock Mechanics Parameters

To obtain rock mechanics parameters, the shear wave travel time must first be determined [57,58]. However, measuring shear wave travel time is both costly and complex, resulting in the widespread practice of measuring only longitudinal wave travel time [37]. The longitudinal and shear wave velocities were determined in this study. Therefore, a conversion relationship between shear wave (v_p) and longitudinal wave (v_s) velocities was established (Figure 8), thereby forming a regional empirical conversion formula:

$$v_s = v_p \times 0.732 - 484.28 \quad (10)$$

where v_p is the longitudinal velocity; v_p is the shear wave velocity, m/s.

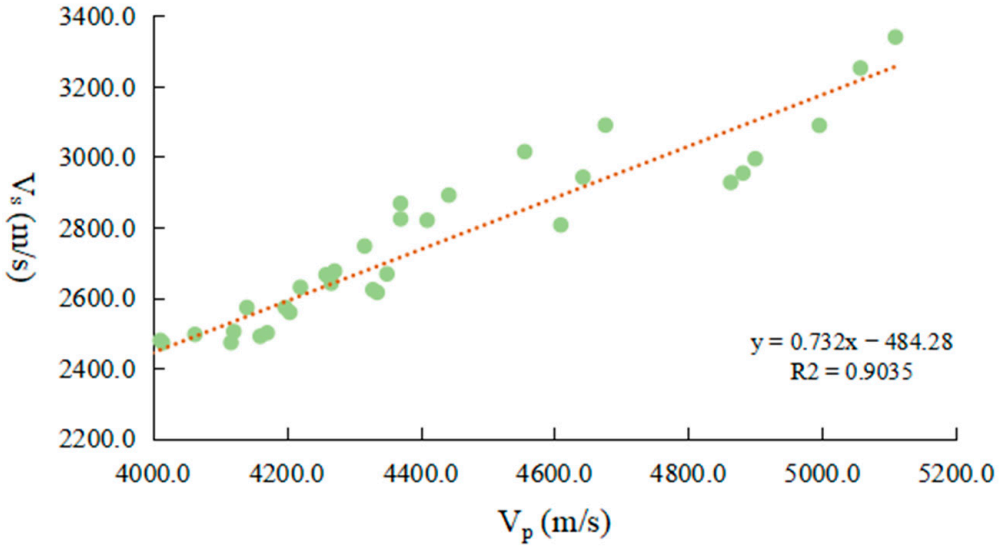


Figure 8. Conversion relationship between longitudinal and transverse wave velocities.

The distribution range of static Young's modulus measured experimentally is 11–15 GPa, while the dynamic Young's modulus varies between 34 and 48 GPa. The discrepancies between these datasets are significant and necessitate correction. Fitting analysis reveals a correlation coefficient of 0.7287, indicating a strong positive correlation (Figure 9).

$$E_s = 05952 \times E_d - 9.477 \quad (11)$$

where E_s is the static Young's modulus, GPa; E_d is the dynamic Young's modulus, GPa.

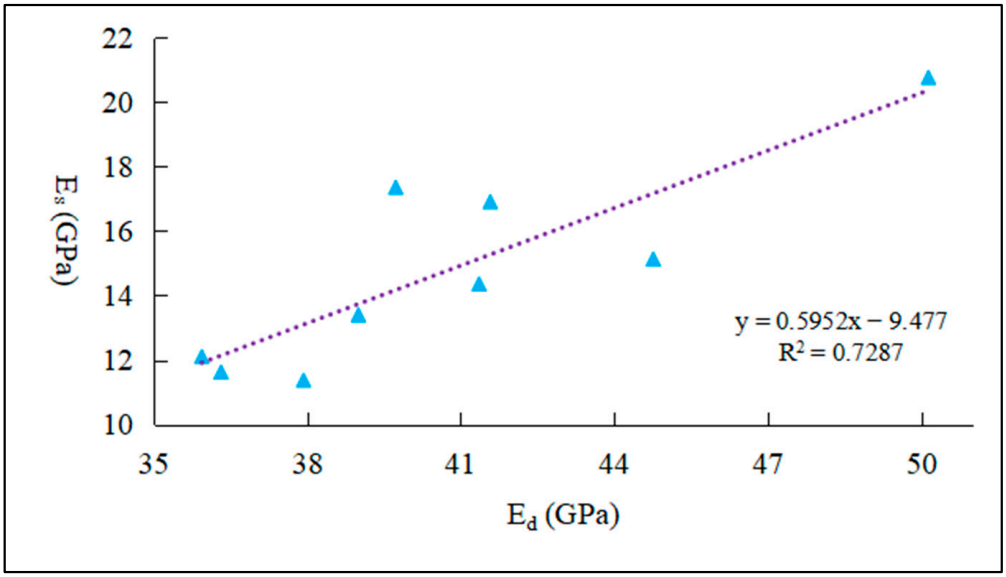


Figure 9. Conversion relationship between dynamic and static Young's modulus.

The range of the static Poisson's ratio is 0.14–0.24, while the dynamic Poisson's ratio ranges from 0.17 to 0.25. The differences between the two ranges are not significant, with the dynamic Poisson's ratio generally exceeding the static Poisson's ratio. Fitting analysis

of static and dynamic Poisson's ratios yields a correlation coefficient of 0.7481, indicating a strong positive correlation between them (Figure 10). The conversion relationship between dynamic and static Poisson's ratios is:

$$\mu_s = \mu_d \times 1.0728 - 0.0345 \quad (12)$$

where μ_s is the static Poisson's ratio; μ_d is the dynamic Poisson's ratio.

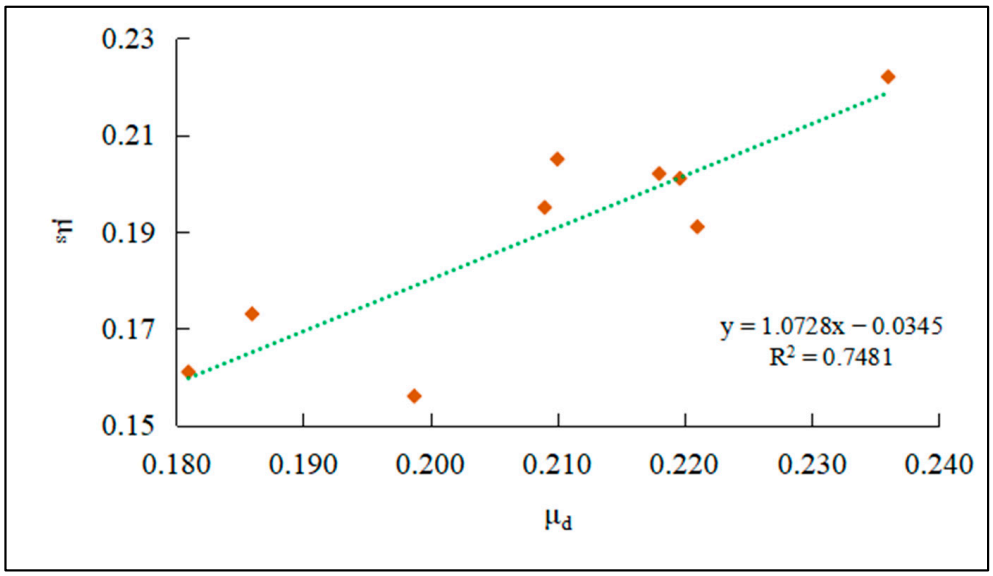


Figure 10. Conversion relationship between dynamic and static Poisson's ratio.

5. Discussions

5.1. The Correlation Between Fracture Linear Density and Thickness of Stratum

There is a correlation between stratum thickness and fracture development. Analysis of the thickness and fracture linear density in tight sandstone from field profiles in the Chang 7 member reveals a negative correlation between fracture linear density and rock layer thickness (Figure 11). Specifically, an exponential relationship is observed between the exposed fracture linear density and rock layer thickness (Figure 12). As rock layer thickness increases, the linear density of fracture decreases. Conversely, a reduction in rock layer thickness corresponds to an increase in fracture linear density. Notably, when the layer thickness exceeds 5.2 m, the change in fracture linear density becomes gradual (Figure 12). However, when the thickness falls below 2.5 m, there is a pronounced variation in fracture linear density.

The observed phenomenon can be attributed to the distribution of external forces across rock layers. In thicker rock layers, the external force is distributed over a larger area, resulting in lower stress at each point. This dispersion of stress reduces the likelihood of fracture formation. Conversely, thinner rock layers experience concentrated stress over a smaller area, making fractures more likely to develop. Therefore, under identical tectonic stress conditions, rock layers with similar lithology are more susceptible to fracture formation as their thickness decreases. Conversely, thicker rock layers tend to exhibit poorer fracture development.

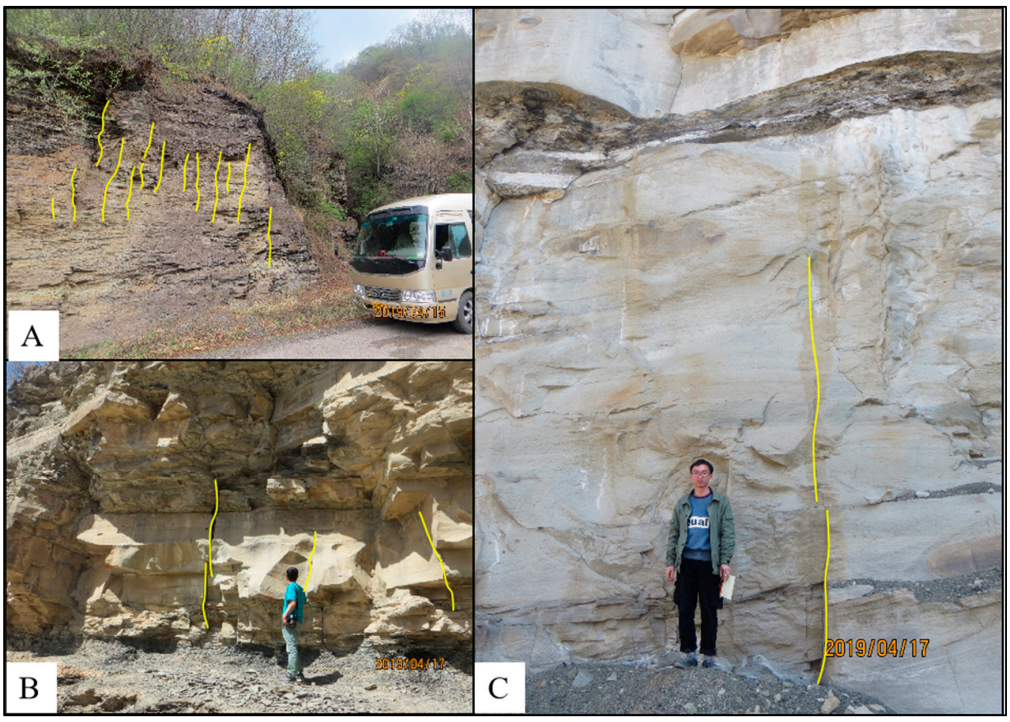


Figure 11. Impact of layer thickness on field fracture development. (**A**) Thin layer thickness leads to well-developed fractures. (**B**) Medium layer thickness results in moderately developed fractures. (**C**) Dense layer thickness results in poorly developed fractures.

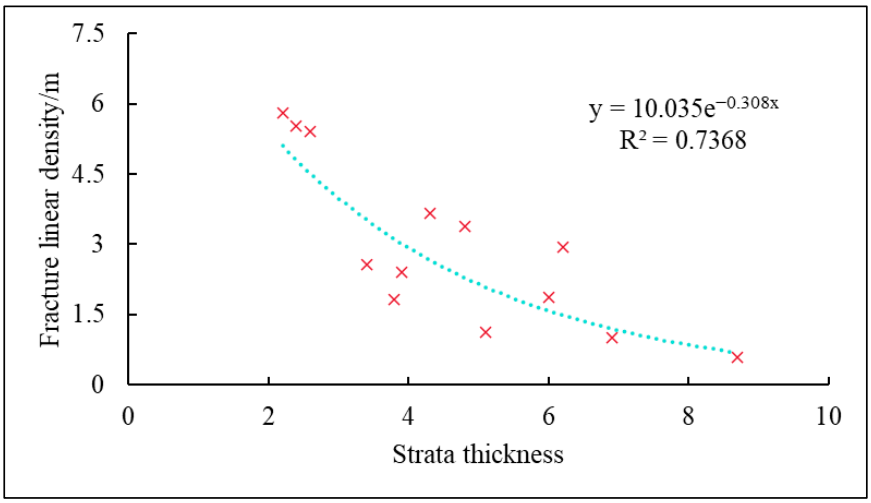


Figure 12. Correlation between fracture linear density and rock layer thickness.

5.2. Fracture Development Characteristics in Various Lithologies

The development of fractures in sedimentary rocks is intricately linked to the inherent properties of the rocks, with variations in lithology resulting in differing mechanical properties. Under external stress, the degree and mode of deformation vary accordingly. Typically, plastic rocks are less prone to fracturing. In the study area, the predominant lithologies include mudstone, silty mudstone, argillaceous sandstone, siltstone, fine sandstone, and medium-grained sandstone, with sandstone and conglomerate being relatively rare. Fractures are most prevalent in siltstone and fine sandstone, followed by mudstone and medium-grained sandstone, with the least development observed in mudstone and silty mudstone (Figure 13). In siltstone and fine sandstone, fracture line density can reach up to 5.2 per meter, whereas in mudstone, it is only 0.4 per meter (Figure 14). This variation

is attributed to the fact that in brittle formations (i.e., siltstone and fine sandstone), stress is often released through fracturing, whereas in softer formations, stress is absorbed, reducing the likelihood of fracture formation.

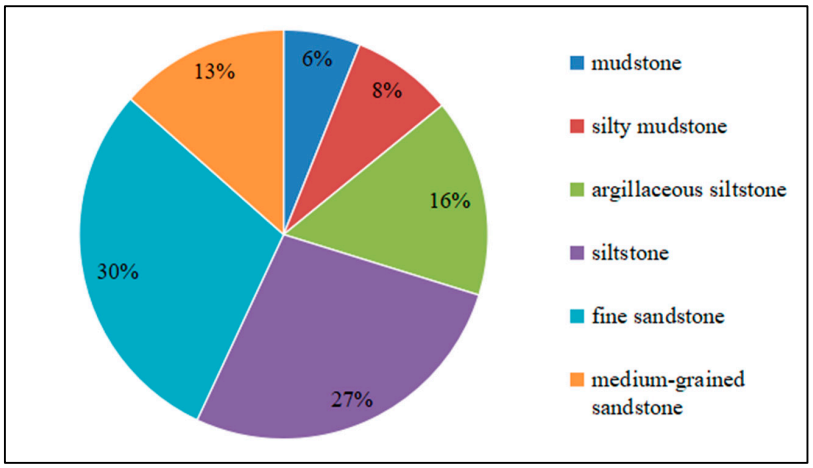


Figure 13. Frequency map of fracture development in various lithologies.

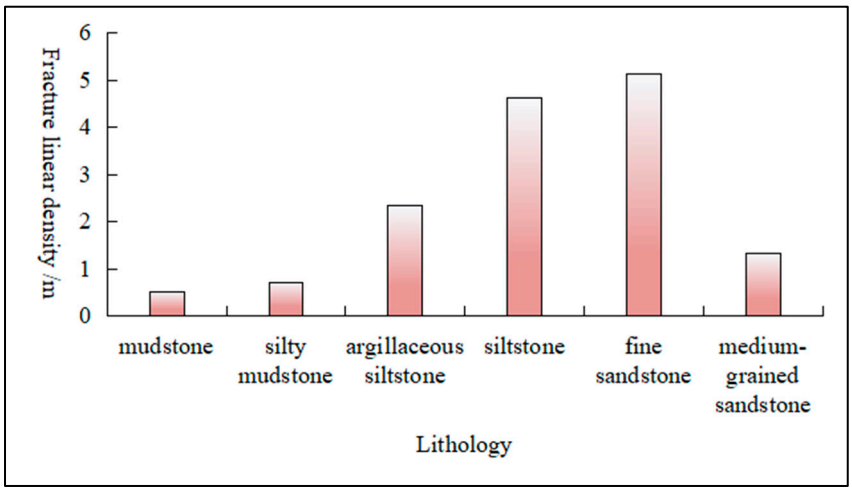


Figure 14. Histogram of fracture linear density distribution across different lithologies.

5.3. The Relationship Between Brittleness Index and Fracture Parameters

The brittleness index is directly related to a rock's ability to generate fractures, with higher brittleness indicating a greater potential for complex fracture networks [58]. However, the effect of the brittleness index on the geometry of fracture development remains uncertain. To address this, the relationships between fracture length, aperture, dip angle, linear density, and brittleness index were statistically analyzed. The analysis reveals that as the brittleness index increases, both fracture linear density and length generally rise (Figure 15A,B). This trend is attributed to the higher Young's modulus and lower Poisson's ratio associated with greater rock brittleness, which facilitates the formation of complex fracture networks. Conversely, fracture aperture is negatively correlated with the brittleness index (Figure 15C). This inverse relationship may result from the dense fracture network in highly brittle formations, which leads to reduced spacing and smaller apertures for individual fractures. Although there is a positive correlation between fracture dip angle and brittleness index, this correlation is weak (Figure 15D). This weak correlation may be attributed to the fact that the primary factors influencing dip angles are regional tectonic activity, while the brittleness index has little effect on predicting fracture orientation.

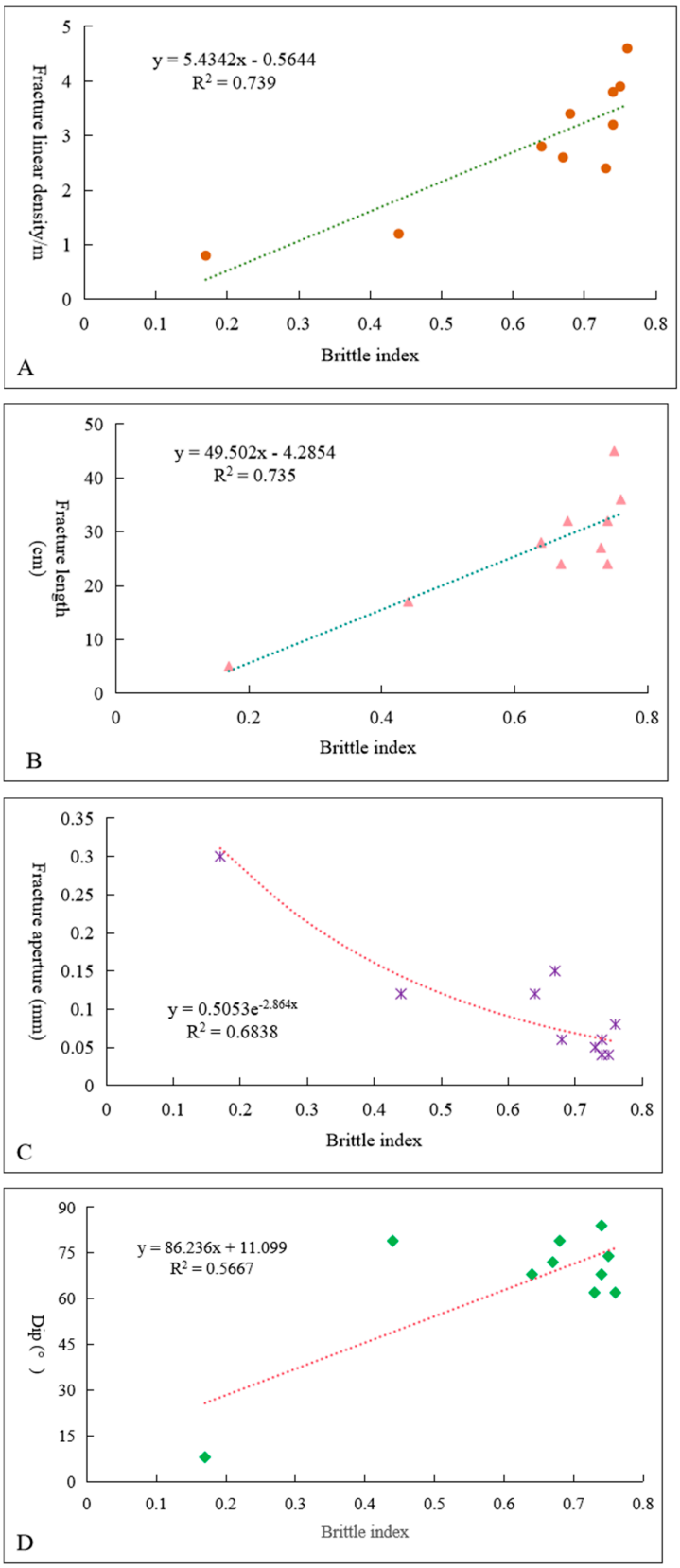


Figure 15. Correlation between fracture parameters and brittleness index. (**A**) The relationship between fracture linear density and brittleness index. (**B**) The association between fracture length and the brittleness index. (**C**) The connection between fracture aperture and the brittleness index. (**D**) The correlation between fracture dip and brittleness index.

5.4. Rock Mechanical Stratigraphy

Using the conversion relationship between static and dynamic rock mechanics parameters, the continuous logging curve of static Young's modulus and Poisson's ratio was derived, demonstrating a negative correlation between these two mechanical parameters; that is, a higher Young's modulus corresponds to a lower Poisson's ratio. The distribution of static Young's modulus ranges from 12 to 27 GPa, while static Poisson's ratio ranges from 0.14 to 0.24 (Figure 16). The brittleness index was calculated based on Formulas (7)–(9), revealing that the brittleness index was quite high overall. In Chang 7_1 and Chang 7_2, the brittleness index generally exceeds 0.6, while a decline in brittleness index is observed at the bottom of Chang 7_3.

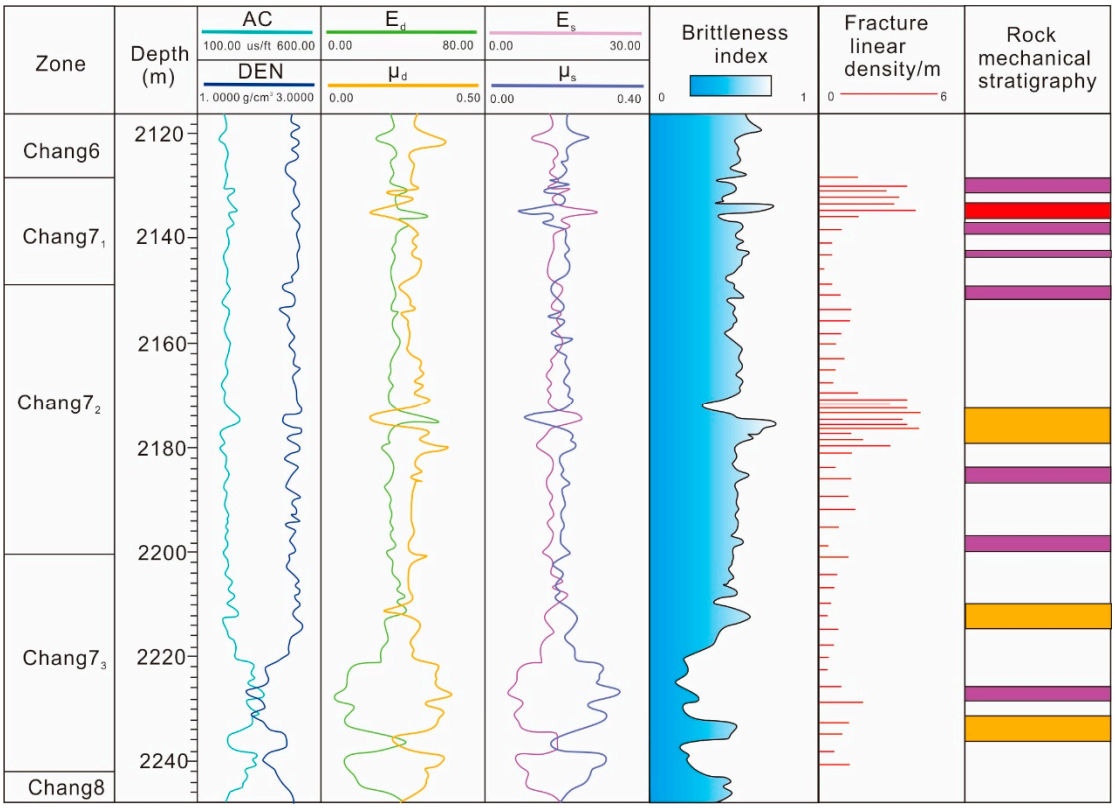


Figure 16. Mechanical stratigraphy classification by rock mechanics parameters (the red, orange, and purple colors in column 8 indicate the first, second, and third categories, respectively, while white indicates the fourth category).

Based on the calculated results of layer thickness and brittleness index, rock mechanics layers can be classified into four categories. The first category includes layers with a high brittleness index and small thickness (Figure 16). The second category encompasses layers with a high brittleness index and medium thickness. The third category covers layers with a medium brittleness index and small thickness. All other combinations are classified as the fourth category. The results indicate that the rock mechanics layers in the study area predominantly fall into the first three categories, which are associated with well-developed fractures.

6. Conclusions

(1) The fracture development in the Chang 7 member of the Yanchang Formation indicates that the majority of fractures are structural, predominantly occurring as shear fractures. Observations of rock cores indicate that the majority of fractures are high-angle or vertical, with fewer instances of horizontal or bedding fractures. The length of these fractures ranges between 20 and 30 cm, and their aperture is generally concentrated

between 0.05 and 0.5 mm. Most fractures are either filled or partially filled, which is advantageous for subsequent oil and gas accumulation. Microscopic examination of rock thin sections and scanning electron microscopy shows the presence of intragranular, intergranular, and transgranular fractures, which facilitate later dissolution and transformation processes for oil and gas. Imaging logging reveals a predominance of dark colors over bright colors, suggesting that most fractures in the study area are unfilled.

(2) A comprehensive analysis of fracture response characteristics resulted in the selection of acoustic logging, natural potential logging, and caliper logging, which were assigned weights of 0.5, 0.3, and 0.2, respectively. The comprehensive probabilistic index P_f effectively identified the fracture development sections at 2135–2140 m and 2173–2181 m, demonstrating high recognition accuracy.

(3) The thickness of rock layers exhibits a negative correlation with fracture linear density, following an exponential relationship. When the thickness of the exposed layer exceeds 5.2 m, the amplitude of variation in fracture line density becomes minimal. Additionally, the brittleness index influences fracture development; both the length and linear density of fractures are positively correlated with the brittleness index, while the fracture aperture shows a negative correlation. The inclination angle of fractures displays a weak positive correlation with the brittleness index.

(4) Fractures are most extensively developed in fine sandstone and sandstone, whereas they are absent in mudstone. Additionally, the development of fractures is influenced by the rock mechanics layer; fractures are most pronounced in the first, second, and third types of rock mechanics layers, while the fourth type of rock mechanics layer exhibits no developed fractures.

Author Contributions: Conceptualization, P.C., S.Y. and X.C.; methodology, P.C. and S.Y.; validation, S.Y. and X.C.; formal analysis, P.C. and X.C.; data curation, P.C., Z.L. and X.C.; writing—original draft preparation, P.C. and X.C.; writing—review and editing, P.C., C.S. and H.Q.; visualization, P.C. and Z.L.; supervision, C.S. and H.Q. All authors have read and agreed to the published version of the manuscript.

Funding: This work was supported by National Major Science and Technology Projects of China (grant number: 2016ZX05046-003).

Institutional Review Board Statement: Not applicable.

Informed Consent Statement: Not applicable.

Data Availability Statement: The data presented in this study are available on request from the corresponding author.

Acknowledgments: We express our gratitude to PetroChina Company Limited for providing the necessary data.

Conflicts of Interest: The authors declare no conflict of interest.

References

1. Dorhjie, D.B.; Mukhina, E.; Kasyanenko, A.; Cheremisin, A. Tight and Shale Oil Exploration: A Review of the Global Experience and a Case of West Siberia. *Energies* **2023**, *16*, 6475. [CrossRef]
2. Hu, B.; Pu, J.; Li, C.H. Experimental investigation on the influence factors of primary production performance of tight oil. *Pet. Sci. Technol.* **2022**, *40*, 2179–2192. [CrossRef]
3. Tang, Y.; Lv, Z.X.; He, W.J.; Qing, Y.H.; Song, X.Z.; Cao, Q.M.; Qian, Y.X.; Zhu, T.; Li, N.; Li, X. Characteristics and Genesis of Alkaline Lacustrine Tight Oil Reservoirs in the Permian Fengcheng Formation in the Mahu Sag, Junggar Basin, NW China. *Minerals* **2022**, *12*, 979. [CrossRef]
4. Wang, Z.Z.; Zhang, Z.; Liu, Y.J.; Wei, B.; Lin, X.H. Experimental Study on Porosity & Permeability Characteristics of Typical Tight Oil Reservoirs. *Chem. Technol. Fuels Oils* **2024**, *60*, 80–87. [CrossRef]
5. Lyu, W.Y.; Zeng, L.B.; Lyu, P.; Yi, T.; Dong, S.Q.; Wang, S.J.; Xu, X.; Chen, H. Insights into the mechanical stratigraphy and vertical fracture patterns in tight oil sandstones: The Upper Triassic Yanchang Formation in the eastern Ordos Basin, China. *J. Pet. Sci. Eng.* **2022**, *212*, 110247. [CrossRef]

6. Guo, Q.H.; Li, S.X.; Jin, Z.K.; Zhou, X.P.; Liu, C.L. Characteristics and exploration targets of Chang 7 shale oil in Triassic Yanchang Formation, Ordos Basin, NW China. *Pet. Explor. Dev.* **2023**, *50*, 878–893. [CrossRef]
7. Bai, B.; Hao, J.Y.; Fu, L.; Liu, Y.X.; Wang, J.P.; Wang, L.; Taylor, K.G.; Ma, L. Microfacies and diagenetic alteration in a semi-deep to deep lacustrine shale: The Yanchang Formation in the Ordos Basin, China. *Pet. Sci.* **2024**, *21*, 1524–1538. [CrossRef]
8. Wang, L.Y.; Li, S.H. Geological Modeling of Shale Oil in Member 7 of the Yanchang Formation, Heshui South Area, Ordos Basin. *Appl. Sci.* **2024**, *14*, 6602. [CrossRef]
9. Zhou, X.F.; Wei, J.G.; Zhao, J.F.; Zhang, X.Y.; Fu, X.F.; Shamil, S.; Abdumalik, G.; Chen, Y.H.; Wang, J. Study on pore structure and permeability sensitivity of tight oil reservoirs. *Energy* **2024**, *288*, 129632. [CrossRef]
10. Yang, Y.; Liao, G.Z.; Xiong, W.; Shen, R.; Zhang, J.; Li, Q.; Wang, S.Z.; Zhang, J.Z.; Tan, L.F.; Shao, G.Y. Physical and numerical simulation of inter-fracture flooding in heterogeneous tight oil reservoirs. *Energy Rep.* **2022**, *8*, 12970–12978. [CrossRef]
11. Qu, G.Z.; Su, J.; Zhao, M.; Bai, X.J.; Yao, C.J.; Peng, J. Optimizing Composition of Fracturing Fluids for Energy Storage Hydraulic Fracturing Operations in Tight Oil Reservoirs. *Energies* **2022**, *15*, 4292. [CrossRef]
12. Hao, L.W.; Ma, X.F.; Gao, W.Q.; Ren, Z.C.; Tao, H.F.; Huang, W.K. Geochemical Characteristics of the Chang 7 Source Rocks of the Triassic Yanchang Formation in Ordos Basin, China: Implications for Organic Matter Accumulation and Shale Oil Potential. *Energies* **2022**, *15*, 7815. [CrossRef]
13. Wang, S.L.; Li, H.; Lin, L.F.; Yin, S. Development Characteristics and Finite Element Simulation of Fractures in Tight Oil Sandstone Reservoirs of Yanchang Formation in Western Ordos Basin. *Front. Earth Sci.* **2022**, *9*, 823855. [CrossRef]
14. Zhu, H.H.; Zhang, Q.X.; Dong, G.D.; Shang, F.; Zhang, F.Y.; Zhao, X.M.; Zhang, X. Characteristics and control factors of feldspar dissolution in gravity flow sandstone of Chang 7 Member, Triassic Yanchang Formation, Ordos Basin, NW China. *Pet. Explor. Dev.* **2024**, *51*, 114–126. [CrossRef]
15. Chen, Z.J.; Ji, A.Z.; Yuan, Y.D. Fine Logging Evaluation of Fractures in Continental Tight Oil Sandstone Reservoirs of Yanchang Formation in the Ordos Basin. *Front. Earth Sci.* **2022**, *10*, 860473. [CrossRef]
16. Li, Z.H.; Chen, Z.J.; Yu, L.; Zhang, S.Y.; Gai, K.; Fan, Y.H.; Huo, W.D. Geophysical logging in brittleness evaluation on the basis of rock mechanics parameters: A case study of sandstone of Shanxi formation in Yanchang gas field, Ordos Basin. *J. Pet. Explor. Prod. Technol.* **2023**, *13*, 151–162. [CrossRef]
17. Gao, J.D.; Li, L.R.; Gao, G.R.; Ma, S.W.; Li, M. Fractured Zone Detection Using Petrophysical Logs by Rescaled Windowed R/S Analyses and Discrete Fracture Network (DFN) of Yanchang Formation in Mahuangshan-Hongliugou Area, Ordos Basin, China. *Geofluids* **2023**, *2023*, 9255499. [CrossRef]
18. Qiu, X.L.; Tan, C.Q.; Lu, Y.Y.; Yin, S. Evaluation of fractures using conventional and FMI logs, and 3D seismic interpretation in continental tight sandstone reservoir. *Open Geosci.* **2022**, *14*, 530–543. [CrossRef]
19. He, S.B.; Meng, K.; Wang, C.; Chen, Y.B.; Zhao, H.; Wang, H.Y.; Yu, H.Y. Fracture Identification Using Conventional Logs in Ultra-Low Permeability Sandstone Reservoirs: A Case Study of the Chang 6 Member of the Ordos Basin, China. *Minerals* **2023**, *13*, 297. [CrossRef]
20. Khadivi, K.; Alinaghi, M.; Dehghani, S.; Soltani, M.; Hassani, H.; Mosavi, S.C.; Shiralipour, M.; Fardin, H.; Sanjari, S.; Partovi, M. Integrated fracture characterization of Asmari reservoir in Haftkel field. *J. Pet. Explor. Prod. Technol.* **2022**, *12*, 1867–1887. [CrossRef]
21. Sun, S.S.; Huang, S.P.; Gomez-Rivas, E.; Griera, A.; Liu, B.; Xu, L.L.; Wen, Y.R.; Dong, D.Z.; Shi, Z.S.; Chang, Y.; et al. Characterization of natural fractures in deep-marine shales: A case study of the Wufeng and Longmaxi shale in the Luzhou Block Sichuan Basin, China. *Front. Earth Sci.* **2023**, *17*, 337–350. [CrossRef]
22. Xue, Y.C.; Wang, L.J.; Zhao, X.L.; Tian, H. The Fractured Model Study of Low-Permeability Reservoir in Xinli Oil Field. *Front. Earth Sci.* **2022**, *10*, 841456. [CrossRef]
23. Zhang, P.F.; Lu, S.F.; Li, J.Q.; Wang, J.J.; Zhang, J.J.; Chen, G.; Huang, H.S.; Zhi, Q.; Yin, Y.J. Microscopic characteristics of pore-fracture system in lacustrine shale from Dongying Sag, Bohai Bay Basin, China: Evidence from scanning electron microscopy. *Mar. Pet. Geol.* **2023**, *150*, 106156. [CrossRef]
24. Wang, J.F.; Yang, C.; Liu, Y.K.; Xiong, Y.Q. Nanoindentation investigation of mechanical and creep properties of continental Triassic Yanchang Formation shale, Ordos Basin. *Interpret.—A J. Subsurf. Charact.* **2022**, *10*, SJ29–SJ41. [CrossRef]
25. Wang, Z.N.; Luo, X.R.; Liu, K.Y.; Lei, Y.H.; Zhang, L.K.; Cheng, M.; Wang, X.Z. Evaluation of pore-scale wettability in the tight sandstone reservoirs of the Upper Triassic Yanchang Formation, Ordos Basin, China. *Mar. Pet. Geol.* **2022**, *138*, 105528. [CrossRef]
26. Xiao, Z.L.; Lu, J.G.; Li, Y.; Zhang, H.X.; Chen, S.J. Oil generated overpressure of shale and its effect on tight sandstone oil enrichment: A case study of Yanchang Formation in the Ordos Basin, China. *J. Pet. Sci. Eng.* **2022**, *219*, 111120. [CrossRef]
27. Zheng, R.H.; Wang, Y.F.; Li, Z.P.; Zhang, Z.H.; Wang, G.L.; Zhang, H. Differences and origins of hydrocarbon generation characteristics between mudstone and shale in the Seventh Member of the Yanchang Formation, Ordos Basin, China. *Int. J. Coal Geol.* **2022**, *257*, 104012. [CrossRef]
28. Wang, X.; Fu, G.M. Formation water geochemistry and the petroleum geological significance in Yanchang Formation of Wuqi Oilfield, Ordos Basin, China. *Int. J. Oil Gas Coal Technol.* **2023**, *32*, 93–102. [CrossRef]
29. Fu, Z.; Lu, S.F.; Wang, H.J. A new method for identifying micro fractures and characterizing fractures of different scales. *Front. Earth Sci.* **2023**, *10*, 1018106. [CrossRef]

30. Li, Q.H.; Ren, D.Z.; Wang, H.; Sun, H.P.; Li, T.; Zhang, H.P.; Yan, Z.; Zhang, R.J.; Qu, L. Microscopic characteristics of tight sandstone reservoirs and their effects on the imbibition efficiency of fracturing fluids: A case study of the Linxing area, Ordos Basin. *Energy Geosci.* **2024**, *5*, 100302. [CrossRef]
31. Das, G.; Biswas, S.K.; Mondal, T.K.; Mondal, S. Evolution of tensile fractures in feldspar porphyroclast and its implication in paleostress estimation. *J. Struct. Geol.* **2024**, *179*, 105039. [CrossRef]
32. Dong, S.Q.; Zeng, L.B.; Du, X.Y.; Bao, M.Y.; Lyu, W.; Ji, C.Q.; Hao, J.R. An intelligent prediction method of fractures in tight carbonate reservoirs. *Pet. Explor. Dev.* **2022**, *49*, 1364–1376. [CrossRef]
33. Hussein, H.S. Carbonate fractures from conventional well log data, Kometan Formation, Northern Iraq case study. *J. Appl. Geophys.* **2022**, *206*, 104810. [CrossRef]
34. Hasan, M.L.; Tóth, T.M. Multiple linear regression and gene expression programming to predict fracture density from conventional well logs of basement metamorphic rocks. *J. Pet. Explor. Prod. Technol.* **2024**, *14*, 1899–1921. [CrossRef]
35. Tian, Y.K.; Zhou, F.J.; Hu, L.Q.; Liu, H.T. Quantification of rock heterogeneity and application in predicting rock mechanical properties. *Bull. Eng. Geol. Environ.* **2023**, *82*, 401. [CrossRef]
36. Wu, Z.H.; Yang, C.; Zuo, Y.J.; Lou, Y.L.; Song, H.L.; Cui, H.T.; Tang, M.T. Effect of natural fractures on mechanical properties and fracture patterns of shale at microscopic scale: An example from the Lower Cambrian Niutitang formation in Qianbei region. *Geomech. Geophys. Geo-Energy Geo-Resour.* **2024**, *10*, 42. [CrossRef]
37. Yang, S.Q.; Yang, J.; Mu, Z.L.; Liu, G.J.; Huang, M.; Li, K.S.; Huang, Y.H. Experimental Study on Mechanical Behavior, Fracture Characteristics, and Acoustic Emission Damage Characteristics of Sandstone Under Triaxial Multistage Stress Disturbance. *Rock Mech. Rock Eng.* **2024**, *57*, 8633–8655. [CrossRef]
38. Available online: https://openstd.samr.gov.cn/bzgk/gb/newGbInfo?hcno=037A6660E50EAAFC966E598146286715 (accessed on 22 October 2024).
39. Available online: https://openstd.samr.gov.cn/bzgk/gb/newGbInfo?hcno=59A5D1BC04922E03C10E620FD8789057 (accessed on 22 October 2024).
40. Zhang, R.; Sun, J.M.; Cheng, Z.G.; Xin, B.X.; Chen, H. Mechanical Behavior and Microstructural Characteristics of Ultradeep Tight Carbonate Rocks With Different Burial Depths. *Front. Earth Sci.* **2022**, *10*, 858899. [CrossRef]
41. Cai, M.; Wang, Y.; Zhao, W.C.; Shi, X.D.; Li, T. Study on Local Brittleness of Rock Based on Multiple Linear Regression Method: Case Study of Shahejie Formation. *Geofluids* **2023**, *2023*, 6189068. [CrossRef]
42. Chen, K.; Cudmani, R.; Peña, A. Assessment method for determining rock brittleness based on statistical damage constitutive relations. *Geomech. Energy Environ.* **2024**, *37*, 100517. [CrossRef]
43. Gong, F.Q.; Wang, Y.L. A New Rock Brittleness Index Based on the Peak Elastic Strain Energy Consumption Ratio. *Rock Mech. Rock Eng.* **2022**, *55*, 1571–1582. [CrossRef]
44. Li, H.T.; Chapman, D.N.; Faramarzi, A.; Metje, N. The Analysis of the Fracturing Mechanism and Brittleness Characteristics of Anisotropic Shale Based on Finite-Discrete Element Method. *Rock Mech. Rock Eng.* **2024**, *57*, 2385–2405. [CrossRef]
45. Talkhouncheh, M.Z.; Davoodi, S.; Larki, B.; Mehrad, M.; Rashidi, S.; Vasfi, M. A new approach to mechanical brittleness index modeling based on conventional well logs using hybrid algorithms. *Earth Sci. Inform.* **2023**, *16*, 3387–3416. [CrossRef]
46. Wang, J.; Du, J.H.; Li, W.P.; Chen, X.H.; Zhang, H.; Wang, T.; Li, Z.; Hao, R.Q. Brittleness index evaluation of gas-bearing sandstone under triaxial compression conditions. *Geomech. Geophys. Geo-Energy Geo-Resour.* **2023**, *9*, 160. [CrossRef]
47. Li, Y.M.; Li, J.L.; Wu, Y.H.; Zhao, G.F. Extracting Rock Parameters Through Digital Drilling Test. *Rock Mech. Rock Eng.* **2024**, *57*, 8215–8241. [CrossRef]
48. Noori, M.; Khanlari, G.; Sarfarazi, V.; Rafiei, B.; Nejati, H.R.; Schubert, W. Experimental test and numerical simulation of the effect of brittleness on the microfracturing of sandstone. *Bull. Eng. Geol. Environ.* **2022**, *81*, 309. [CrossRef]
49. Nouri, M.; Khanlari, G.; Rafiei, B.; Sarfarazi, V.; Zaheri, M. Estimation of Brittleness Indexes from Petrographic Characteristics of Different Sandstone Types (Cenozoic and Mesozoic Sandstones), Markazi Province, Iran. *Rock Mech. Rock Eng.* **2022**, *55*, 1955–1995. [CrossRef]
50. Yao, T.Z.; Qian, L.; Mo, Z.G.; Gao, Y.P.; Zhang, J.H.; Zhang, R.; Hu, Q.J.; Xing, X.L. A new brittleness index based on crack characteristic stress and its engineering applications. *Eng. Geol.* **2024**, *330*, 107411. [CrossRef]
51. Zhao, Y.X.; Wang, X.L.; Guo, Y.D.; Danesh, N.N.; Jiang, Y.D. Mechanical properties and brittleness characteristics of sandstone from different burial depths. *Geomech. Geophys. Geo-Energy Geo-Resour.* **2022**, *8*, 165. [CrossRef]
52. Wang, Z.S.; Xiang, H.; Wang, L.B.; Xie, L.; Zhang, Z.G.; Gao, L.F.; Yan, Z.F.; Li, F.L. Fracture Characteristics and its Role in Bedrock Reservoirs in the Kunbei Fault Terrace Belt of Qaidam Basin, China. *Front. Earth Sci.* **2022**, *10*, 865534. [CrossRef]
53. Wang, Z.W.; Zhang, K.; Cheng, Y.H.; Wu, Q.H. Identification and evaluation of fault-fracture reservoirs in buried hills of the Lower Paleozoic, Chengdao area, China. *Energy Geosci.* **2023**, *4*, 100183. [CrossRef]
54. Zhou, Y.; Zhong, X.Q.; Nie, X. Identification and parameter characterization of pores and fractures in shales based on multi-scale digital core data. *Adv. Geo-Energy Res.* **2024**, *13*, 146–160. [CrossRef]
55. Zhang, Y.H.; Ma, J.F.; Wang, Y.; Wang, F.; Li, X.; Zhao, L.X. Quantification of the Fracture Complexity of Shale Cores After Triaxial Fracturing. *Front. Earth Sci.* **2022**, *10*, 863773. [CrossRef]
56. Zhong, W.W.; Zhang, X.; Li, T.; Yang, X.; Deng, W.; Shi, J.C. Study on Microscopic Characteristics of Spatial Distribution of Fractures in Deteriorated Sandstone. *Geofluids* **2022**, *2022*, 7895498. [CrossRef]

57. Sharifi, J.; Nooraiepour, M.; Amiri, M.; Mondol, N.H. Developing a relationship between static Young's modulus and seismic parameters. *J. Pet. Explor. Prod. Technol.* **2023**, *13*, 203–218. [CrossRef]
58. Yang, B.B.; He, M.M.; Wang, H.T.; Zhang, Z.Q.; Zhu, J.W.; Li, N. Experimental investigation on brittleness characteristics of rock based on the ubiquitiformal complexity: Strain rate effect and size effect. *Bull. Eng. Geol. Environ.* **2023**, *82*, 306. [CrossRef]

Disclaimer/Publisher's Note: The statements, opinions and data contained in all publications are solely those of the individual author(s) and contributor(s) and not of MDPI and/or the editor(s). MDPI and/or the editor(s) disclaim responsibility for any injury to people or property resulting from any ideas, methods, instructions or products referred to in the content.